AN EDDY-RESOLVING TECHNIQUE TO PREDICT THE UNSTEADY HORSESHOE VORTEX AND WAKE OF A CYLINDRICAL PIER

GEORGE CONSTANTINESCU, ROBERT ETTEMA, METE KOKEN AND MARIAN MUSTE

IIHR Hydroscience and Engineering, Dept. Civil & Environmental Engrg., University of Iowa, Iowa City, IA 52242-1585, USA

The paper reports on the preliminary findings of two well-resolved (no wall functions) LES simulations of the flow past a circular cylinder (Re_D = 5,000) on a flat bed. In the first simulation, a steady laminar (Blasius) profile is specified at the inflow and no turbulent fluctuations are present. In the second simulation, the fields corresponding to a pre-calculated fully turbulent channel flow simulation are fed through the inflow section in a time-accurate fashion. Attention is focused on the visualization of the unsteady horseshoe vortex (HV) structure around the cylinder and the analysis of the spectral content of the flow in the HV system and wake regions. For the flow conditions considered in the laminar case it is found that the HV system is characterized by the regular shedding of small secondary vortices from the separation region and merging of these vortices with the primary vortex. The structure of HV system in the turbulent case was characterized by the formation of a large primary vortex that oscillates rather chaotically. In the wake region, the flow away from the bed is similar to the one observed for the flow past infinitely long cylinders, while near the bed the turbulent structures that populate the near-wall region interact with the vortex tubes in the detached shear layers and modify the spectral content of the flow.

1 Introduction

Though many studies have focused on scour-depth prediction for bridge piers, only a modest few have looked at the highly turbulent flow fields causing scour (e.g., Baker, 1980, Dargahi, 1990). Better understanding of the flow fields will aid scour-prediction accuracy. This paper uses a leading numerical-modeling technique (large-eddy simulation [LES]) to obtain insights into the flow field generated by a circular cylinder protruding from a flat bed in a shear flow.

Prominent flow features associated with the formation of a scour hole around a cylinder are the necklace-like vortical structure, commonly known as the horseshoe vortex (HV), and the wake eddies shed by the cylinder. Regardless of the exact form of the bridge pier, one the main mechanisms (Baker, 1979, 1980, Dargahi, 1989, 1990) that drive the formation and future evolution of the scour hole is the HV system. To understand how scour develops and rigorously estimate scour depths, it is necessary to describe these flow structures, and to quantify their effect on the river bed near the cylinder base. They cause local sharp increases in turbulence intensity near the pier base. For movable-bed base, these increases significantly contribute to scour. In this paper we are interested in studying especially the HV system and wake at the start of the scouring process (flat bed conditions). Further research steps entail repeating these simulations for bathymetries corresponding to different stages of scour development until equilibrium conditions.

2 Need for an eddy-resolving numerical model

Though recent experimental investigations using Particle Image Velocimetry (PIV) and Laser Doppler Velocimetry (LDV) techniques have increased considerably the understanding of the intricate structure of the flow field generated by a cylinder on a flat plate, a detailed quantitative description of the flow field around the cylinder is lacking. In this regard, use of eddy-resolving numerical simulations offer a promising alternative. Steady RANS simulations can predict only a steady horseshoe vortex and an average wake structure. Even unsteady RANS (URANS) simulations that may capture some of the large scale deterministic unsteadiness in bridge pier flows are unable to predict the evolution of the coherent structures and their effect on bed-sediment transport. Therefore, RANS and URANS simulations are essentially unsuited for predicting scour depths.

A further requirement for capturing these complex flow phenomena is the use of turbulence models that do not employ wall-functions. There are known deficiencies in the wall-function approach in the case when massive separation, adverse pressure gradients and vortex shedding dominate the flow field in the regions of interest.

Moreover, the use of very fine meshes is required especially in the HV region, and for boundary layers and wakes. The mesh sizes required for well-resolved simulations using LES can be of the order of millions cells for relatively low Reynolds numbers. Some important reductions in the mesh size requirements can be obtained by using accurate solvers using unstructured grids with hybrid elements, multi-block methods with non-identical interfaces or Chimera grid methods. The above arguments make a strong case for the use of parallel numerical algorithms that run efficiently on supercomputers or large PC clusters. Even the most advanced simulations of these flows (e.g., Paik et al., 2004, who used URANS with wall functions on grids with around 1 million cells, or Tseng et al., 2000, who used LES with a constant-coefficient Smagorinsky model with wall functions on meshes with around 300,000 cells) fail to satisfy at least one of the above mentioned requirements for simulating the main aspects of bridge-pier flows.

This paper describes two well-resolved LES simulations of flow past a circular cylinder attached to a flat bed flow of relatively low Reynolds number: $Re_D = UD/\nu$ = 5,000 (Re_H = 6,000, D = pier diameter, H = channel depth, U = bulk channel velocity). In the first simulation (case 1) the HV system is laminar, meaning that the flow in the approaching boundary layer is laminar at the separation line upstream of the pier. In the second simulation (case 2) the boundary layer is turbulent at the separation line and the HV system is turbulent. The simulations provide preliminary findings of a series of simulations of flow around a circular cylinder, and concentrate on the visualization of the unsteady HV system and turbulent wake, the calculation of the spectral content of these regions, and their variation with the inflow characteristics of the flow. The writers are still conducting a detailed study of the statistics for the mean velocity and turbulent stress components as well as a detailed study of the variation of the HV system and coherent structures in the turbulent wake with the Reynolds number and pier shape. Sediment

transport processes, such as entrainment and deposition of sediment are not considered in the present study, though the writers intend to use the data collected as part of the present research to explain some experimental observations related to sediment transport.

3 Numerical solver and grid generation

LES is better suited than RANS for predicting flows dominated by coherent turbulence structures, of which junction flows (e.g., flow around bridge piers and abutments) are a perfect example. Unfortunately, the numerical methods used in RANS or even URANS solvers are not directly applicable to LES. RANS typically uses dissipative formulations in discretizing the nonlinear terms to make the algorithm robust. This approach, though, is not suitable for accurate LES solutions. On the other hand, in LES the dissipative scales of motion are not resolved on the grid, thus the use of non-dissipative (central-differences) discretizations leads to numerical instability. Robust LES methods for complex geometries with non-dissipative schemes require non-dissipative schemes that discretely conserve kinetic energy. The parallel LES code employed for the present study (Mahesh et al., 2004) uses a collocated, finite-volume scheme on unstructured grids with arbitrary elements and a dynamic Smagorinsky sub-grid scale model. All operators in the finite-volume formulation are discretized using central-difference schemes. A novelty of the present approach is a new fractional-step algorithm for incompressible flows that is discretely energy conserving on hybrid unstructured grid, thus facilitating simulations at high Reynolds numbers without use of numerical dissipation. The code was validated for both internal and external flows.

The typical grid cell dimensions in the HV system region are 2-3 wall units in the bed normal direction and 5-7 wall units in the other directions, close to DNS requirements. The first cell off the wall is situated at about 0.5 wall units. The grid in the region close to the bottom wall is fine enough to resolve the turbulent streaks. In both simulations the grid and Reynolds number are identical. The same is true for all the boundary conditions with the exception of the inflow conditions. In case 1 (laminar inflow) a constant profile (no fluctuations) corresponding to a Blasius profile with a momentum thickness of 0.3D was specified in the inlet section, while in case 2 (turbulent inflow) the profiles corresponding to a time-accurate LES solution of the fully developed flow in a channel of identical section are used to specify the inflow boundary condition. The time step was 0.002D/U. Statistics were computed over approximately 100D/U to insure convergence. The simulation was run on 16 processors (3.06GHz) of a Xeon PC cluster.

4 Results

4.1. Horseshoe vortex system

Instantaneous streamlines and out-of-plane vorticity fields in the symmetry plane, $\phi = 0^0$, and in an inclined plane (polar angle of $\phi = 45^0$) were used to examine the structure and evolution of the HV system for a laminar (Figs 1-3) and a turbulent (Figs 4-6) incoming boundary layer.

Though in case 1 the structure of the HV system varies with the polar angle (compare Figs 1 and 2), the process is quasi-periodical and takes place over the whole length of the necklace primary vortex. In the $\phi = 0^0$ plane, this period corresponds to the time between two successive mergings (pairings) between the primary vortex PV1 and the next incoming secondary vortex (SV1 in Figs. 1a-f). Sometimes secondary vortices merged first with each other before merging with the primary vortex. This scenario in case 1 corresponds to what is called the regular shedding subsystem of the periodical oscillatory regime. The structure of the HV system in the $\phi = 45^0$ plane is somewhat different. The shedding of secondary vortices does not seem to occur near the separation line, rather secondary vortices appear to form periodically just upstream of the primary vortex and then to merge with the primary vortex. In Fig. 3 the dominant peak in the spectra of the streamwise and vertical velocity components in the HV region is predicted at St = 0.43. The spectrum of the spanwise velocity component in the $\phi = 0^0$ plane displays only one energetic frequency (St = 0.22). Smaller peaks corresponding to the second (St = 0.86) and third (St = 1.30) harmonics are observed. These harmonics appear because of nonlinear interactions primarily inside the primary vortex. The predicted value of the main Strouhal number seems to agree well with the values measured by Wei et al. (2001) in a related study of the flow over square cylinders (St~0.4). Baker (1979) observed that for Re_D~5,000 two main frequencies were present, a high frequency oscillation (St~0.4) and a low frequency oscillation (St~0.26). Based on his discussion and analysis one can associate the higher component with the main frequency (St = 0.43) observed consistently in our simulation.

In the turbulent case, the structure of the HV system is very different to the one observed in the laminar case. Fig. 4 shows the presence of a relatively large primary vortex whose size can oscillate considerably. The position of the separation line is also changing in time, for instance it can vary between x/D = -2.5 and x/D = -1.1 in contrast to case 1 where it was practically constant in time (x/D = -1.8). Even though the shedding of secondary vortices from the separation region is still observed (SV1 in Fig. 4a, SV3 and SV4 in Fig. 4f), the periodicity observed in the laminar case is totally lost. Sometimes these secondary vortices are destroyed before merging with the primary vortex (Figs. 4a-b), at other times two consecutive secondary vortices can merge together as they are advected toward the primary vortex. This is the case observed in Figs. 4c-d. The oscillations of the primary vortex in case 2 appear to be stochastic (Figs. 4 and 5). The velocity power spectra inside the primary vortex show some clear peaks corresponding to St = 0.1. Other peaks at St = 0.2, 0.3, and = 0.55-0.8 may be observed in the spectra of the velocity components at several locations inside the HV system. Compared to the spectra obtained in case 1, higher frequency components (up to St = 2.5-3.0) are observed in case 2. The velocity spectra inside the HV system appear to be

broad, confirming the fact that the flow is turbulent. Dargahi (1989) mentions that, at Re_D = 39,000, the band of energetic frequencies in the horseshoe vortices varies from St = 0.058 to 1.15.

4.2. Wake region

Figure 7 is a snapshot of the coherent structures in the detached shear layers visualized using out-of-plane vorticity contours at the free surface (y/D = 1.2) and near the bed (y/D = 0.2) for both simulation cases. It is interesting to note that even though the consideration of a fully developed turbulent flow with resolved fluctuations in case 2 affected greatly the structure and intensity of the HV system upstream the cylinder, due to the overall low Reynolds number of the flow past the cylinder, the separation and transition scenario in case 2 is very similar to that predicted for case 1, meaning that the fluctuations outside the boundary layer that starts forming on the cylinder from the upstream stagnation point are not high enough to force transition of the boundary layer before separation and the associated increase in the separation (polar) angle due to occurrence of the drag crisis. As for laminar boundary layer separation the polar angle corresponding to separation is practically insensitive to the Reynolds number and/or details of free-stream flow, there are no major differences in the downstream flow between the two cases. The influence of the bottom boundary in both cases is to increase the vorticity levels and range of scales present behind the cylinder. The vorticity patterns at the free surface are very similar to those observed for the flow past infinitely long cylinders. The velocity power spectra in Fig. 8 (case 1) and Fig. 9 (case 2) clearly show that the Strouhal number associated with the large scale vortex shedding in the wake is St = 0.22-0.22, in good agreement with measured values for infinitely long cylinders. The energy associated with the large scale shedding is 2-4 times smaller at y/D = 0.2 compared to the levels recorded away from the bed (y/D > 0.6). Near the bed, the turbulent character of the wake is amplified due to the additional vorticity coming from the near-bed region. A consequence is that the width of the wake is smaller at small distances from the bed, an effect captured in our numerical simulation and in agreement with the findings of Dargahi (1989).

In both cases, the shedding of vortex tubes due to the Kelvin-Helmholtz instabilities in the shear layers takes place practically over the whole depth of flow, however as one gets closer to the bed, due to interactions with the ejected vorticity from the bed, the part of the spectrum associated with the shedding inside the detached shear layers becomes broader; e.g., from St = 0.95-1.1 for y/D > 0.5, to 0.95-1.3 at y/D = 0.2 for case 1 (Fig. 6). In case 2, the spectral content of the detached shear layers away from the bed (y/D>0.5) is practically identical to case 1. However, near the bed (y/D = 0.2) the spectrum is broader (St = 0.7-1.3) compared to St = 0.95-1.3 in case 1.

In Fig. 10 the instantaneous total friction velocity ($\sqrt{\tau/\rho}$) contours nondimensionalized by the mean friction velocity corresponding to a turbulent channel flow at Re_H = 6,000 ($u_\tau/U \sim 0.05$) are plotted for case 1 and 2. Some clear differences are observed between the two distributions. In case 1 the region of high bed shear stress

($\sqrt{\tau/\rho}$ /u_τ > 1.8) is larger as it extends between the cylinder (r/D = 0.5) and r/D = 1.1-1.25 for $\phi < 90^0$. The highest values ($\sqrt{\tau/\rho}$ /u_τ ~ 3.0) are predicted in the acceleration region very close to the cylinder walls $30^0 < \phi < 90^0$. The ratio between the skin friction coefficient beneath the primary vortex and far upstream of the separation line is close to 5.5 which is close to the value of 5.0 obtained by Baker (1979) for a similar case setup at Re_D = 2,610. In case 2 the corresponding dimensions of the zone of high stress are reduced in the upstream part (r/D = 0.9-1.1) mainly because the primary horseshoe vortex is closer to the cylinder (it oscillates around r/D = 1.0 in case 2). Small areas of high stress ($\sqrt{\tau/\rho}$ /u_τ ~ 3.0-4.0) are observed in the region corresponding to the detached shear layers. In fact, we suspect those pockets are just the trace corresponding to the vortices shed in the detached layers. Relative high bed stress values are observed over all horizontal extent of the turbulent wake which explains why a loose bed will be strongly deformed behind the cylinder over large distances downstream.

4.3. RANS vs. LES for flow past a circular pier

We also tried to assess the predictive abilities of one of the most popular commercial software packages (Fluent) which is commonly used for bridge pier flow predictions (e.g., Salaheldin et al., 2004). The linear-SST RANS model was used. The mesh size was close to 1.2 million cells and the first grid point off the walls was situated at $y_1^+ \sim 1$. Second-order upwind discretizations were used for the convective terms. When the simulation was run in time-accurate mode (URANS), the predicted solution was practically steady in the whole domain, and the formation of horseshoe vortices was not captured in the upstream flow. This can be observed from Fig. 11a which shows the streamlines in the $\phi = 0^0$ plane and contours of the out-of-plane vorticity component at the free-surface. The formation of the vortex tubes in the detached shear layers was not captured. This can be attributed to the excessive numerical dissipation present in the code.

We also performed time-accurate laminar simulations at the same Reynolds number using the same inflow profile as in the SST simulation to show that in this particular case, at least for the wake region, suppressing the eddy viscosity introduced by the RANS model (the simulation is more like a coarse DNS with a dissipative code) allowed the unsteadiness to develop both in the detached shear layers and wake (see Fig. 11b). Interestingly, a HV system containing two primary vortices and a floor-attached vortex develops in the upstream flow but they appear to be steady, though both experiments and LES show that the HV system should shed under the conditions considered in the simulation. The reason here is just the numerical dissipation present in the code (in this case Fluent) which locally decreases the effective Reynolds number of the simulation.

5 Conclusions

The flow fields around a surface mounted circular cylinder were investigated in the cases of a developing laminar (Blasius) boundary layer and of a fully turbulent upstream

flow at Re_D = 5,000. The simulations successfully captured the formation of unsteady horseshoe vortices downstream of the separation line. The vortical structure in the laminar case was highly organized and characterized by the shedding of the secondary vortices from the separation region and their subsequent merging with the primary vortex. In the turbulent case, the degree of intermittency was much higher, and the structure of the HV system was found to change significantly in time. Over relatively large time intervals the presence of a large primary vortex that oscillates rather chaotically was observed. The velocity power spectra inside the HV system displayed a wide range of energetic frequencies, up to St = 2.5-3.0. Both simulations show that the structure of the HV system can vary considerably with the polar angle around the cylinder.

As expected, the wake structure away from the bed was similar to the one observed in infinitely long cylinders. However close to the bed, some small differences due to the interactions between the high vortical content of the near bed region and the wake were observed. The simulations accurately captured the formation of the vortex tubes in the detached shear layers (the dominant frequency corresponded to St~1.1) as well as the large scale vortex shedding in the wake (St = 0.2-0.22). The instantaneous bed shear stress distributions in the HV region were found to differ considerably between the two cases. In the case of the turbulent HV system, the positions of the areas of high instantaneous bed-shear stress were closer to the cylinder base, while in the near wake region pockets of higher stress intensity were observed, especially in the detached shear layers, compared to the case in which the HV system was laminar. Overall the instantaneous distribution of the bed shear stress suggests that sediment transport models which predict entrainment only based on the condition that the mean bed shear stress is larger than a critical stress would not be very accurate when applied to complex junction flows. We think that successful prediction of sediment transport and scour should use models that can account for the turbulence characteristics near the bed including the effect of coherent structures, intensity of the turbulence fluctuations and take into account the temporal variability in the distribution of the bed shear stress at least in a statistical way. Use of accurate eddy-resolving techniques which have the ability to capture these phenomena as part of the simulation will reduce the amount of modeling needed in the equations that describe the sediment transport and bed evolution.

The present simulations demonstrate that an accurate LES model can effectively complement the information obtained from experimental studies (especially using PIV techniques) toward understanding the complex flow field structure present in flow past bridge piers, in particular the mechanisms that govern the formation of the horseshoe vortices and the wake-boundary layer interaction downstream of the body. It was also found that URANS is not suitable for prediction of junction flows if a detailed study of the coherent structures and frequency spectra inside the HV system is of interest. The next step will be to calculate detailed mean statistics and to study the variation of the structure of the HV system with the Reynolds number and the shape of the pier.

References

Baker, C. J. (1979). "The laminar horseshoe vortex" *J. Fluid Mech*., 95(2), 347-367.

Baker, C. J. (1980). "The turbulent horseshoe vortex" *J. Wind Engineering and Industrial Aerodynamics*, 6, 9-23.

Dargahi, B. (1989). "The turbulent flow field around a circular cylinder" *Expt. Fluids*, 8, 1-12.

Dargahi, B. (1990). "Controlling mechanism of local scouring" *J. Hydr. Engrg.*, 116(10), 1197-1214.

Mahesh, K., Constantinescu, S.G. and Moin, P. (2004). "A numerical method for large eddy simulation in complex geometries" *J. Computational Physics*, Vol. 197, 215-240.

Paik, J., Ge, L., and Sotiropoulos, F. (2004). "Toward the simulation of complex 3D shear flows using unsteady statistical turbulence models" *Int. J. Heat and Fluid Flow*, in press.

Salaheldin, T. M., Imran, J., and Chaudhry, M. H. (2004). "Numerical modeling of three-dimensional flow field around circular piers" *J. Hydr. Engrg.*, 130(2), 91-100.

Tseng, M. H., Yen, C. L., and Song, C. C. S. (2000). "Computation of three-dimensional flow around square and circular piers" *Int. J. Numerical Methods in Fluids*, 34, 207-227.

Wei, Q. D., Chen, G., and Du, X. D. (2001). "An experimental study on the structure of juncture flows*" J. Visualization*, 3(4), 341-348.

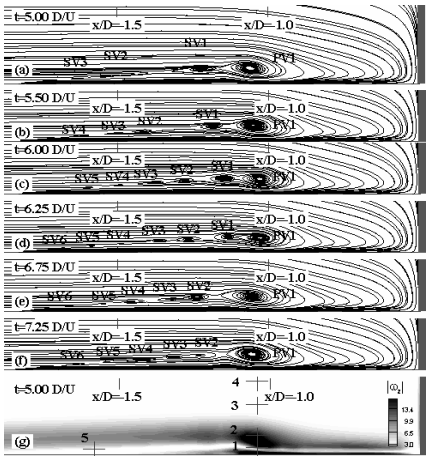

Figure 1. Instantaneous streamlines in the symmetry plane z = 0 for case 1 showing the time evolution of the HV system (a) –(f) streamlines; (g) t = 5.00D/U, $|\omega_z|$D/U.

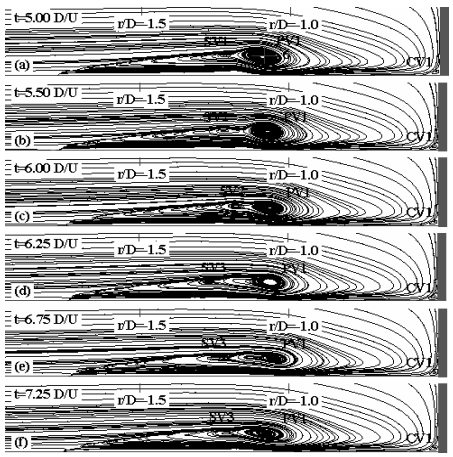

Figure 2. Instantaneous streamlines in an inclined plane corresponding to a polar angle of $\phi = 45^0$ for case 1 showing the time evolution of the HV system.

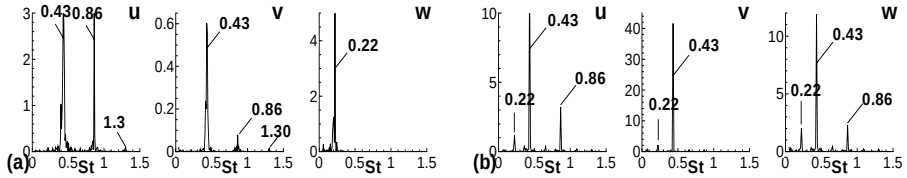

Figure 3. Power spectra of the velocity components in the horseshoe vortex system for case 1 (a) Point 2 (z=0); (b) Point 6 (ϕ =45^0). The position of the points is shown in Figures 1 and 2.

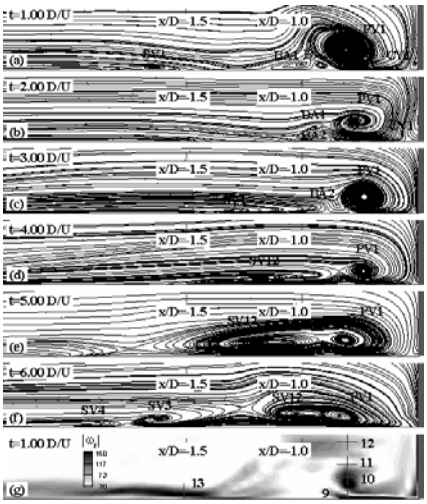

Figure 4. Instantaneous streamlines in the symmetry plane z=0 for case 2 showing the time evolution of the HV system (a)-(f) streamlines; (g) t=1.00D/U, | ω_z|D/U.

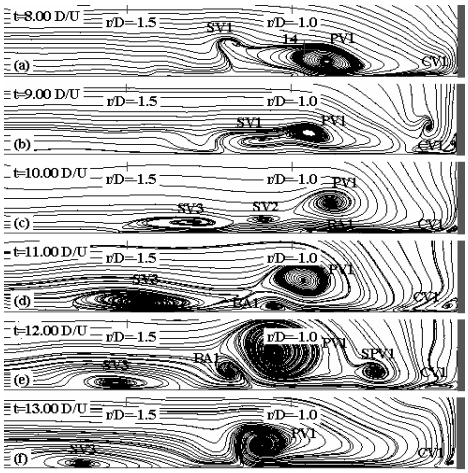

Figure 5. Instantaneous streamlines in an inclined plane corresponding to a polar angle of ϕ =45^0 for case 2 showing the time evolution of the HV system.

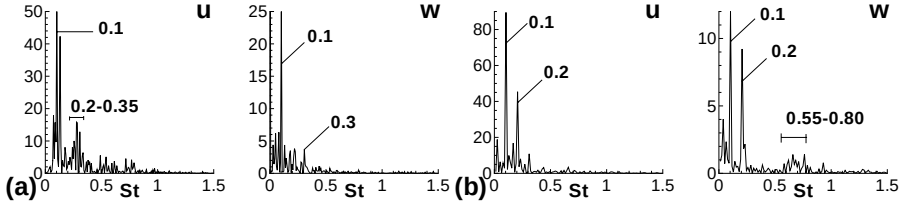

Figure 6. Power spectra of the velocity components in the horseshoe vortex system for case 2 (a) Point 10 (z=0); (b) Point 14 (ϕ =45^0). The position of the points is shown in Figures 4 and 5.

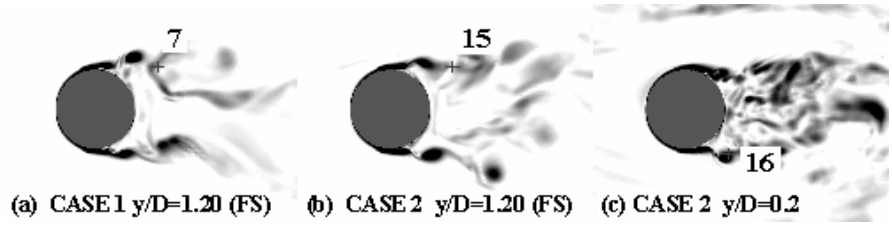

Figure 7. Instantaneous vorticity magnitude contours | ω_t|D/U at the free surface (y/D = 1.2) and close to the bed (y/D = 0.2) showing the vortical structures in the detached shear layers.

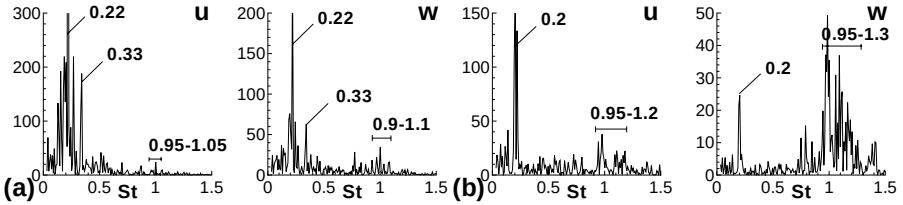

Figure 8. Power spectra of the velocity components in the cylinder wake (detached shear layers) for case 1 (a) Point 7 (free surface y/D = 1.2); (b) Point 8 (near the bed, y/D = 0.2). Position of points indicated in Figure 16a.

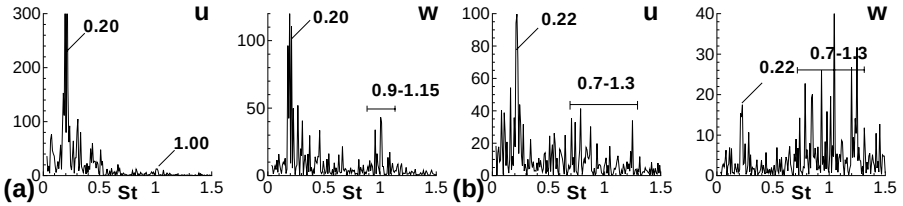

Figure 9. Power spectra of the velocity components in the cylinder wake (detached shear layers) for case 2 (a) Point 15 (free surface y/D = 1.2); (b) Point 16 (y/D = 0.2). Position of points indicated in Figure 16b.

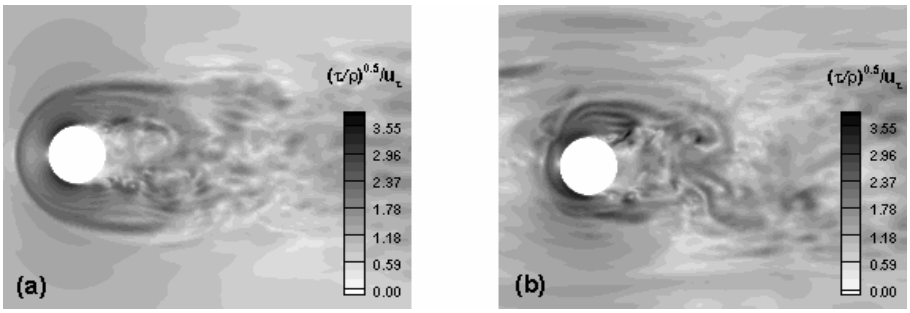

Figure 10. Contour plot of the instantaneous total friction velocity ($\sqrt{\tau/\rho}$) nondimensionalized by the mean friction velocity corresponding to a turbulent channel flow at Re_H = 6,000 (u_τ/U~0.05) (a) case 1; (b) case 2.

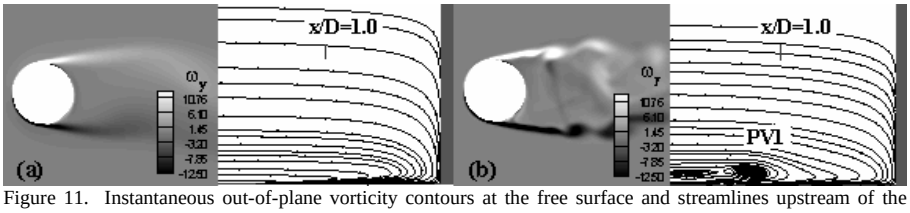

Figure 11. Instantaneous out-of-plane vorticity contours at the free surface and streamlines upstream of the cylinder in the ϕ = 0 plane obtained from time-accurate Fluent simulations (a) SST model (b) laminar.